frontiers | Frontiers in Chemistry

TYPE Original Research
PUBLISHED 08 August 2023
DOI 10.3389/fchem.2023.1215619

OPEN ACCESS

EDITED BY
Xiao Feng,
Beijing Institute of Technology, China

REVIEWED BY
Magdalena Warczak,
University of Technology and Life Sciences in Bydgoszcz, Poland
Ali Benvidi,
Yazd University, Iran

*CORRESPONDENCE
Wilbert Mtangi,
wmtangi@cut.ac.zw
Massimo Innocenti,
m.innocenti@unifi.it

†These authors have contributed equally to this work

RECEIVED 02 May 2023
ACCEPTED 27 July 2023
PUBLISHED 08 August 2023

CITATION
Kawondera R, Bonechi M, Maccioni I, Giurlani W, Salzillo T, Venuti E, Mishra D, Fontanesi C, Innocenti M, Mehlana G and Mtangi W (2023), Chiral "doped" MOFs: an electrochemical and theoretical integrated study.
Front. Chem. 11:1215619.
doi: 10.3389/fchem.2023.1215619

Chiral "doped" MOFs: an electrochemical and theoretical integrated study

Rufaro Kawondera[1†], Marco Bonechi[2†], Irene Maccioni[2], Walter Giurlani[2,3], Tommaso Salzillo[4], Elisabetta Venuti[4], Debabrata Mishra[5], Claudio Fontanesi[3,6], Massimo Innocenti[2,3,7]*, Gift Mehlana[8] and Wilbert Mtangi[1]*

[1]Institute of Materials Science, Processing and Engineering Technology, Chinhoyi University of Technology, Chinhoyi, Zimbabwe, [2]Department of Chemistry, University of Firenze, Firenze, Italy, [3]National Interuniversity Consortium of Materials Science and Technology (INSTM), Firenze, Italy, [4]Department of Industrial Chemistry "Toso Montanari", University of Bologna, Bologna, Italy, [5]Department of Physics and Astrophysics, University of Delhi, New Delhi, India, [6]Department of Engineering "Enzo Ferrari" (DIEF), University of Modena, Modena, Italy, [7]Center for Colloid and Surface Science (CSGI), Florence, Italy, [8]Department of Chemical Sciences, Midlands State University, Gweru, Zimbabwe

This work reports on the electrochemical behaviour of Fe and Zn based metal-organic framework (MOF) compounds, which are "doped" with chiral molecules, namely: cysteine and camphor sulfonic acid. Their electrochemical behaviour was thoroughly investigated via "solid-state" electrochemical measurements, exploiting an *"ad hoc"* tailored experimental set-up: a paste obtained by carefully mixing the MOF with graphite powder is deposited on a glassy carbon (GC) surface. The latter serves as the working electrode (WE) in cyclic voltammetry (CV) measurements. Infrared (IR), X-ray diffraction (XRD) and absorbance (UV-Vis) techniques are exploited for a further characterization of the MOFs' structural and electronic properties. The experimental results are then compared with DFT based quantum mechanical calculations. The electronic and structural properties of the MOFs synthesized in this study depend mainly on the type of metal center, and to a minor extent on the chemical nature of the dopant.

KEYWORDS

metal-organic framework, chiral doping, cyclic voltammetry, solid state electrochemistry, SEM, XRD

Highlights

1. Synthesis of Fe and Zn MOFs doped with chiral molecules
2. Electronic properties via "solid-state" electrochemical measurements
3. Development of a specially adapted electrochemical cell
4. Morphological and compositional characterisation (IR, XRD, SEM, EDS)

1 Introduction

Metal-organic frameworks (MOFs) have attracted increasing scientific interest due to unique features including; high specific surface area, high crystallinity, exceptional and tuneable pore size (Ghanbari et al., 2020; Wang and Astruc, 2020). In fact, the opportunity to synthesize porous materials with high modularity and diverse functionality makes MOFs

suitable candidates for solid-state materials in electronic applications (Zhao et al., 2020). Moreover, the physical and chemical properties of MOFs can be customized and designed through a suitably tailored synthesis (Li et al., 2016). Thus, due to these special characteristics and exceptional tunability, MOFs differ from traditional porous materials (silica, activated carbon and zeolites) and are promising candidates for application also in sensors and catalysis. In general, MOFs are assembled from metal cations and organic linkers via metal-ligand coordination bonds (James, 2003; Zhou and Kitagawa, 2014). In recent years, scientists have conducted intense research in the production of chiral MOFs (and covalent MOFs, CMOFs) (Gong et al., 2022). In this arena, chiral MOFs are of particular interest because of their specific field of application which includes; chiral enantioselective recognition (Zhao et al., 2017; Han et al., 2019; Niu et al., 2022), enantioselective separation (Padmanaban et al., 2011; Peng et al., 2014; Abbas et al., 2018), asymmetric catalysis (Wang et al., 2011; Bhattacharjee et al., 2018; Dybtsev and Bryliakov, 2021), and sensing (Wanderley et al., 2012; Yang et al., 2021). These peculiar features can be exploited in crystal engineering, optoelectronics, medicine, biology, pharmacology, and environmental science. In particular, chirality within MOFs can be induced exploiting all of the different constituent components, i.e., linker, metal node, or even guest molecules (Ma et al., 2022). The presence of guest molecules embedded within the MOF structure as well as the functionalization of cavities, can induce chiral properties within the overall MOF architecture (Sharifzadeh et al., 2021). In general, there are three ways to obtain chiral MOFs. i) Chirality can be generated during crystal growth thanks to the nature and physical structure of precursors (Altaf et al., 2022). This approach leads to the crystallization of MOFs in a chiral space group because the spatial disposition of achiral building block has an enantiospecific supramolecular interaction. This method shows some difficulties, because the use of achiral components often leads to a final racemization of the system (Zhang et al., 2008). ii) The second method for obtaining chiral MOFs involves the use of chiral likers (Kutzscher et al., 2016). This procedure is a direct method of "chiralization" and there are interesting examples where this strategy results in chiral MOFs showing unique properties (Gedrich et al., 2011; Sawano et al., 2015). On the other hand, the use of chiral linkers may require the development of specific synthesis leading to increased costs and possibly environmental issues due to the substances used. iii) The third approach is an indirect method that leads to the formation of achiral frameworks and utilization of some external chiral agents to produce stereogenic centres (Xue et al., 2016; Zavakhina et al., 2019). Chiral inducing compounds may involve chiral guest, solvent, auxiliary pendant or functionalization (Gheorghe et al., 2021). In this last case the presence of an enantiopure chiral agent is the driving force that induces chirality. This third strategy allows simple, inexpensive molecules to be included in the framework without changing the initial synthesis of the MOF. In electrochemistry, MOFs are a class of promising candidates for electrode surface functionalization and have the potential to extend the application range of electrochemical sensors (Ma et al., 2020). Indeed, many papers can be found in the literature dedicated to the development of MOF-based electrochemical sensors (Guo et al., 2016; Gonçalves et al., 2021; Daniel et al., 2022), in particular for the detection of heavy metal ions in aqueous solutions (Tran et al., 2020). In addition to the previously mentioned fields of application, MOFs are also emerging materials in the field of electrocatalysis (Nivetha et al., 2019; Mukhopadhyay et al., 2020; Yang et al., 2020), thanks to their electrochemical properties (Zhang et al., 2014; Jiang et al., 2021; Yang et al., 2022), which are comparable to those of systems used in water splitting and Oxygen Reduction Reaction (ORR) (Passaponti et al., 2020; Savastano et al., 2020; Bonechi et al., 2021a; Giurlani et al., 2022a). Remarkably, the effective use of chiral surfaces in the water splitting process, concerning the Oxygen Evolution Reaction (OER), has already been demonstrated in the recent past (Mtangi et al., 2015; Mtangi et al., 2017; Garcés-Pineda et al., 2019; Gazzotti et al., 2020). Thus, chiral MOFs appear to be promising materials for use in the water splitting process. Indeed, Fe-based and Zn-based MOFs are a well-known class of compounds. Among the iron-based MOFs, the most common is MIL53(Fe), obtained by a combination between iron(III) cations and 1,4-dicarboxylic acid, eventually yielding a 3D network (or secondary building units) which contain FeO_6 hexagonal chains and dicarboxylate anions (Sudik et al., 2005; Scherb et al., 2008; Ajpi et al., 2023). MIL53(Fe) shows significant advantages compared with other MOFs, which include chemical stability (Chen et al., 2017; Le et al., 2019), the presence of iron (a nontoxic and widely available metal) and a green and sustainable manufacturing process (Millange and Walton, 2018; Navarathna et al., 2020). Zn-based MOFs are also an interesting class of MOFs as they exhibit structural features similar to those of MIL53(Fe). They have a network consisting of Zn(II) cations tetrahedrally coordinated by two molecules of 1,4-dicarboxylic acid and two molecules of N,N'-bis (pyridin-4-methyl) cyclohexane-1,4-diamine (Altaf et al., 2018).

In this study, Fe based and Zn based MOFs were synthesized and characterised by using spectroscopic techniques: infrared spectroscopy (FT-IR), X-ray diffraction (XRD), and scanning electron microscope (SEM). MIL53(Fe) and Zn MOF derivatives "doped" with chiral molecules were prepared using a simple, ecologically-friendly method, and characterized via X-ray diffraction and spectroscopic experiments. In this work, eight different MOFs are studied. MIL53 (Fe based MOF) where the framework features 1,4-dicarboxylic acid as linker, is named (MIL53). MIL53 (Fe based MOF) where the framework features aminoterephthalic acid as linker, is named NH2 MIL53. MIL53 (Fe based MOF) with a moderate addition of L-cysteine, R-camphorsulfonic acid and S-camphorsulfonic acid, are named MIL53 L-Cys, MIL53 R-CSA and MIL53 S-CSA, respectively. A Zn based MOF where the framework features 1,4-dicarboxylic acid and N′-N bis(pyridin-4-ylmethylene)cyclohexane-1,4-diamine (bpcda) as linkers, is named (Zn-MOF). A Zn based MOF where the framework features aminoterephthalic acid as linker, is named (NH_2-ZnMOF). Zn based MOFs with a moderate addition of L-cysteine, R-camphorsulfonic acid and S-camphorsulfonic acid, are named Zn-MOF L-Cys, Zn-MOF R-CSA and Zn-MOF S-CSA, respectively. L-cysteine, R-camphorsulfonic acid and S-camphorsulfonic acid were selected as the preferred chiral linkers because of their small chain length.

In particular, the electrochemical behaviour was studied by performing cyclic voltammetry (CV) measurements using a solid-state electrochemical approach (Solano et al., 2021; Solano et al., 2022). Typically, electrochemical-based CV measurements are

exploited to study the electrochemical behaviour of metals and organic compounds in bulk solution (Bonechi et al., 2021b; Stefani et al., 2021; Giurlani et al., 2022b; Bonechi et al., 2022), or using commercial systems of the electroplating industry (Berretti et al., 2020; Mariani et al., 2022; Comparini et al., 2023). In this study we adopted a new custom-designed setup to probe the crystal electrochemical behaviour, to avoid the dissolution of the solid-state material. The experimental results have been compared with data obtained by using DFT based quantum mechanical calculations.

2 Experimental

2.1 Chemicals

All chemicals and reagents were analytical grade. N′N dimethylformamide (DMF) and Zinc Nitrate were purchased from ACE Chemicals, South Africa. Titanium (IV) oxide nanoparticles (21 nm primary particle size), Fluorine doped tin oxide (FTO) (surface resistivity of ~7Ω/sq) coated glass substrates, ethanol, acetone, Iron(III) chloride $FeCl_3{\cdot}6H_2O$, terephthalic acid H_2BDC (benzene-1,4-dicarboxylic acid), 2-aminoterephthalic acid H_2N-BDC (2-aminobenzene-1,4-dicarboxylic acid), ethanol, L-cysteine, R-camphorsulfonic acid, S- camphorsulfonic acid, acetonitrile, graphite powder (<20 μm) and potassium chloride (KCl) were purchased from Sigma, Germany and used with no further purification. Aqueous solutions were prepared using milliQ water.

2.2 Instrumentation

Original Fe and Zn based doped MOFs (eight different compounds) were synthesized in a Digital oven, Labotec EcoTherm Economy Oven, South Africa. Details concerning the synthesis are reported in the Supporting Information. Infrared measurements were performed using the FT-IR spectrometer, Perkin-Elmer Spectrum Two, United States, equipped with a transmission mode interferometer Dynascan, Perkin-Elmer, United States. IR spectra were recorded in the range 400–4,000 cm^{-1} with a spectral resolution of 2 cm^{-1} and 32 scans. Powder X-ray diffraction (PXRD) measurements were carried out using a Bruker D2 phaser XRD machine, United States, with DIFFRAC-SUITE software for controlling the instrument and analyzing the data. Scanning electron microscope (SEM) images were investigated using a Scanning Electron Microscope, SU3800, Hitachi, Japan, equipped with an EDS detector UltimMax, Oxford instrument, United Kingdom. For PXRD measurements MOF were immobilised on a copper surface by dropcast of an acetonitrile dispersion dried in a nitrogen stream. UV-Vis spectra were recorded by using a UV-1900i Shimadzu UV-Vis Spectrophotometer using 1 cm path length polystyrene cuvette for photocatalytic measurements. CH Instruments Electroanalyser model 608E and electrochemical workstation (potentiostat/galvanostat) PGSTAT204, Metrohm AutoLab, Switzerland, were used to perform electrochemical measurements, driven by Nova2.1 software.

2.3 Synthesis of MOFs

2.3.1 Synthesis of MIL53 and NH2 MIL53.

1.35 g of $FeCl_3{\bullet}6H_2O$ and linkers were dissolved in 25 mL DMF. The amount of linker corresponding to 0.85 g of H_2BDC for the synthesis of MIL53 and 0.93 g of NH2-BDC for the synthesis of NH2 MIL53. The mixture was then transferred into a Teflon-lined autoclave and heated up at 150°C for 6 h. The yellow solid was extracted, refluxed with DMF for 12 h. After filtering the solid was washed with C_2H_5OH for three times (3 mL × 10 mL), and then dried at 80°C.

2.3.2 Synthesis of chiral MIL53 derivatives

In the case of chiral derivatives, 0.04 g of L-Cysteine was added to the reaction vessel for the synthesis of MIL53 L-Cys, 0.06 g of R-camphorsulfonic acid for the synthesis of MIL53 R-CSA, 0.06 g of S-camphorsulfonic for the synthesis of MIL53 S-CSA. The procedure used for the synthesis of MIL-53 was used for the synthesis of the chiral MIL-53. The quantities for $FeCl_3{\bullet}6H_2O$, H2BDC and DMF remained the same in all the MIL-53 derivatives.

2.3.3 Synthesis of Zn-MOF

To obtain the Zn-MOF, the synthesis of the linker agent N,N'-bis(pyridin-4-ylmethyl)cyclohexane-1,4-diamine (BPCDA) was first carried out. 4-Pyridylcarboxyldehyde (5 g) and (1R,4R)-cyclohexane-1,4-diamine (5.33 g) was added to ethanol (30 mL). Then, triethylamine (7.08 g) was added slowly and refluxed for 4 h. After refluxing, the reaction mixture was cooled down to room temperature. Portion-wise addition of $NaBH_4$ (4.41 g) was carried out and then the stirring of reaction content was performed overnight at room temperature. 10 mL of water was added to quench the extra reducing agent, while 40 mL of dichloromethane (DCM) was added to separate the organic layer. Repeated extractions with DCM were carried out and the organic layers were combined. The product was dried by removing the organic solvent by using anhydrous Na_2SO_4 through evaporation. Then the synthesis of the zinc-based metal organic framework was carried out. A mixture of $Zn(NO_3)_2{\cdot}6H_2O$ (0.297 g, N,N'-bis(pyridin-4-ylmethylene)cyclohexane-1,4-diamine (bpcda) (0.297 g), H_2BDC (0.172 g) and a mixture of DMF and H_2O (10 mL, v/v: 3/1) was prepared and placed in glass vial. The vial was loosely capped and heated at 105°C for 3 days. White block-shaped crystals were obtained after which the vial was cooled to room temperature, washed in DMF three times (3 × 10 mL DMF) and dried in air.

2.3.4 Synthesis of chiral Zn-MOF derivatives

In the case of Zn-MOF chiral derivatives, 0.0121 g of L-Cysteine was added to the reaction vessel for the synthesis of Zn-MOF L-Cys, 0.0232 g of R-camphorsulfonic acid for the synthesis of Zn-MOF R-CSA, 0.0232 g of S-camphorsulfonic for the synthesis of Zn-MOF S-CSA. The procedure used for the synthesis of ZnMOF was used for the synthesis of the chiral Zn based MOFs. The quantities for $Zn(NO_3)_2{\cdot}6H_2O$, bpcda, H_2BDC and solvent (DMF and water) remained the same in all the Zn based MOF derivatives.

2.4 Electrochemical measurements

The MOF electrochemical behaviour was investigated within the so-called solid-state electrochemical paradigm by using an in-house flat-cell of original design in a typical three-electrodes electrochemical cell set-up. The GCE/MOF served as the working electrode (WE), while a coiled Pt wire and an Ag/AgCl (saturated KCl) electrode served as the counter (CE) electrode and reference electrode (RE), respectively. The special flat-cell configuration of the cell, developed in the past for ECALE depositions (Forni et al., 2000; Innocenti et al., 2001; Giurlani et al., 2018; Salvietti et al., 2018; Giurlani et al., 2020) and adapted for solid-state measurements, features the working electrode placed at the bottom, to help maintaining the graphite-powder/MOF mixture in position. A suitable arrangement was adopted (Supplementary Figure S1), a cylindrical Teflon cell featuring a hole (7 mm diameter) in the bottom was used in a vertical configuration, where the glassy carbon electrode (GC) (1.5 cm diameter) was tightened from below. The GC electrode is held in place by a 1.5 cm diameter screw, which also ensures the electrical contact. A Teflon ring was used to ensure no solution leakage from the cell. The CE and RE were placed at the top of the cylinder in contact with the electrolytic solution. Prior to surface modification, the GC working electrode was polished using 0.05 μm alumina slurries on a polishing cloth; it was cleaned carefully, and then sonicated for 10 min in milliQ water to clean the surface and remove any polishing residue. Finally, the GC working electrode was dried in a nitrogen stream. The effective cell set-up and GC electrode activation procedure was cross-checked by recording CVs in a solution of 1 mM ferricyanide in 0.1 M KCl, in the −0.3 to +0.7 V potential range, we obtained a ΔEp (peak-to-peak separation between the oxidation and reduction potentials) at 25 mVs^{-1} of 60 mV. MOFs crystals (1.0 mg) were placed over the WE and covered with of graphite powder (10.0 mg). A drop of acetonitrile is added to make the mixture compact and then the GC modified electrode was left "to dry" for 10 min in a nitrogen atmosphere. CV measurements were recorded in the −0.8 to +1.2 V potential range vs. Ag/AgCl KCl $_{sat}$. Throughout the paper all the potential values are expressed with reference to the $Ag/AgCl/KCl_{sat}$ reference electrode (RE), unless otherwise stated.

2.5 Preparation and functionalization of FTO/TiO_2/MOFs electrodes.

TiO_2 nanoparticulate films were deposited on fluorine-doped tin oxide, FTO (surface resistivity of ~7 Ω/sq) coated glass, using the electrophoretic deposition (EPD) technique. A suspension of TiO_2 nanoparticles (NPs) was prepared by dispersing 0.4 g TiO_2 NPs in 40 mL of de-ionized water. Prior to making dispersions, TiO_2 nanoparticle powders were heated at 570 K for 1 h. The mixture was stirred overnight to ensure homogeneity. Prior to nanoparticle deposition, the FTO substrates were boiled in acetone for 15 min, followed by 15 min of boiling in ethanol, and finally rinsed with de-ionized water. After rinsing, the substrates were dried in the air for 15 min. Electrophoretic deposition (EPD) was performed with a CHI electrochemical analyser, model 608E, using the Chronopotentiometry mode. During EPD, the suspension was continuously stirred using a magnetic stirrer. After completion of the last cycle, the electrodes were annealed for 2 h at 400K. Functionalization of FTO/TiO_2 surfaces to yield the final FTO/TiO_2/MOF photoelectrodes was achieved by drop casting 20 μL of 1 mM slurry MOF solutions dissolved in ethanol onto the FTO/TiO_2 surfaces. The electrodes were then left to dry under controlled humidity for a period of 3 weeks.

2.6 Theoretical calculations

Calculations were performed in the framework of *ab initio* quantum mechanical based methods with Gaussian (Frisch et al., 2017) and Quantum Espresso (Giannozzi et al., 2009) programs, using C1 symmetry and unrestricted wave function. Chemcraft (Andrienko, 2023) is used to display molecular structures and molecular orbitals. Molecular orbitals were obtained by full optimization carried out at UB3LYP/6-31G(d) levels of theory. Geometry optimization was carried out by using Barone and Cossi's polarizable conductor model (CPCM) (Cossi et al., 2003) to account for N,N-dimethylformamide interaction.

3 Result and discussion

3.1 Solid-state cyclic voltammetry

Figures 1A, B show CV curves recorded for the chiral "doped" MOF MIL53 S-CSA and Zn-MOF S-CSA, respectively. The black solid line is the control CV recorded using graphite powder only, i.e., the "blank" baseline. It must be noted that a prominent capacitive contribution in the—0.7–1.0 V potential range yields a quite regular "rectangular box" CV pattern as depicted in Figures 1A, B. The red solid curves in Figures 1A, B are the CVs recorded after mixing the graphite powder with the chiral MOF (details of the electrode preparation are in the experimental section). The CV of the MIL53 S-CSA MOF features two redox peaks (labelled as Eox and Ered in Figure 1A) centred at about 0.5 V. This suggests that the redox process underlying the presence of the two current peaks in Figure 1A can be assigned to the Fe (III)/Fe(II) redox couple. The peak-to-peak separation is about 0.3 V, which is rather large, such a potential difference is due to the solid-state nature of the electroactive system. Moreover, iron is in an octahedral coordination (a quite stable state environment).

In addition, the overall MOF framework is based on organic molecules which are well known to behave more closely to a dielectric than to a conductive material, this further hinders the Fe(III)/Fe(II) charge transfer kinetics. Supplementary Figure S2 shows the CV curves obtained for the remaining four Fe based MOFs studied in this paper and Supplementary Figure S3 shows the CV curves for ferrocene a well-studied material used as a control and compared with MIL53 S-CSA. Table 1 summarizes the electrochemical results.

Please note the effect of "doping" due to the presence of different organic "dopants". The selected four dopants actually affect the electrochemical behaviour by both shifting the redox peak potential and CV pattern. CSA derivatives induce an overall shift of the peak potential to slightly more positive values, featuring a much prominent quasi-reversible

10.3389/fchem.2023.1215619

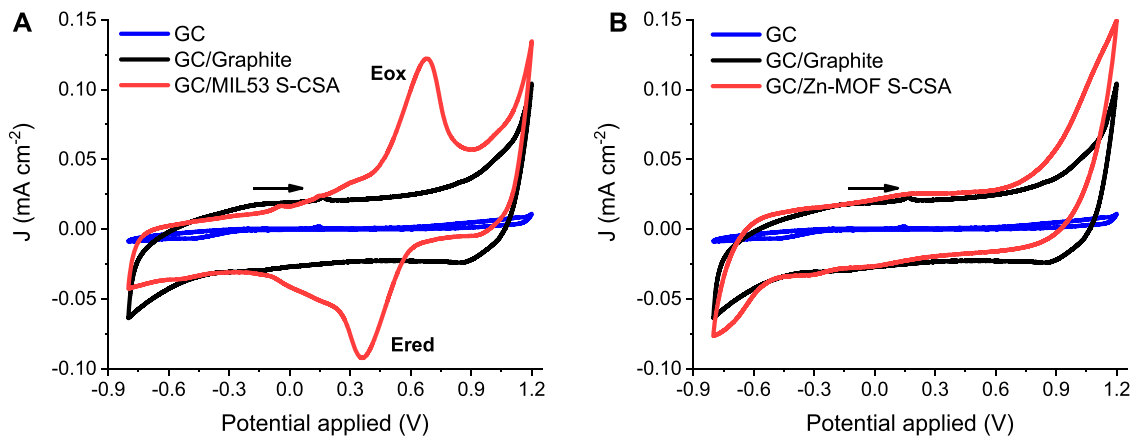

FIGURE 1
CV curves in aqueous 0.1 M KCl, Pt (CE), Ag/AgCl/KCl_{sat}, 10 mV s^{-1} the potential scan rate: **(A)** GC/MIL53 S-CSA (WE) **(B)** GC/Zn-MOF S-CSA (WE).

TABLE 1 Electrochemical results, iron based MOFs.

Compound	Oxidation	Reduction	Difference
	(V)		
MIL53	0.682	0.366	0.316
MIL53 S-CSA	0.676	0.363	0.313
MIL53 R-CSA	0.608	0.418	0.190
NH2 MIL53	0.592	0.408	0.184
MIL53 L-Cys	0.805	0.198	0.607

behaviour. Current peaks are definitively much more symmetric (compare Figure 1A main; Supplementary Figure S2C Supporting Information). A rather peculiar result is obtained in the case of cysteine, where a much broader shoulder is present. This is probably due to the overlap of two/three separate peaks, which suggests the existence of two/three different species formed between iron and cysteine (cysteine features three functional groups able to bind iron, i.e. the thio, amino and carboxylic acid moieties). The electrochemistry of Zn based MOFs is characterized by the absence of any reversible (or quasi-reversible) oxidation/reduction current signal, as it can be seen by the inspection of the CVs shown in Figure 1B, Supplementary Figure S4 in the Supporting Information. In this respect Zn based MOFs appear promising materials, to be used in amperometric sensors, because of very low faradaic currents and large volume/surface ratio. On the other hand, the absence of any faradaic current is a direct proof of the electrochemical stability of the "doping" chiral compounds, cysteine and camphor sulphonic acid.

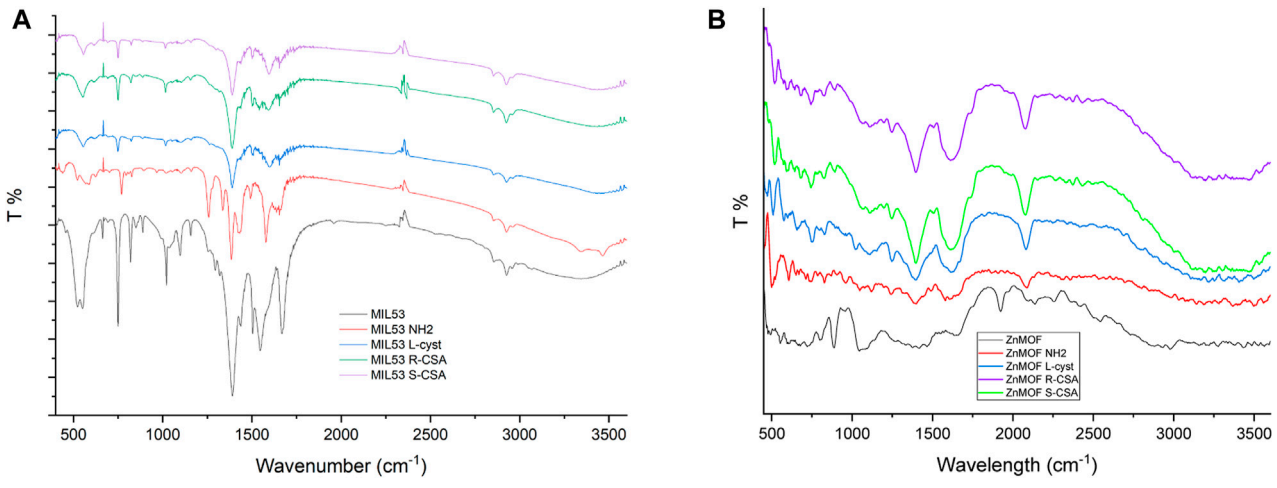

FIGURE 2
(A) Infrared spectra of MIL53 and chiral MIL53 derivatives MOFs recorded in KBr pellet. **(B)** Infrared spectra of Zn-MOF and chiral Zn-MOF derivatives recorded in KBr pellet.

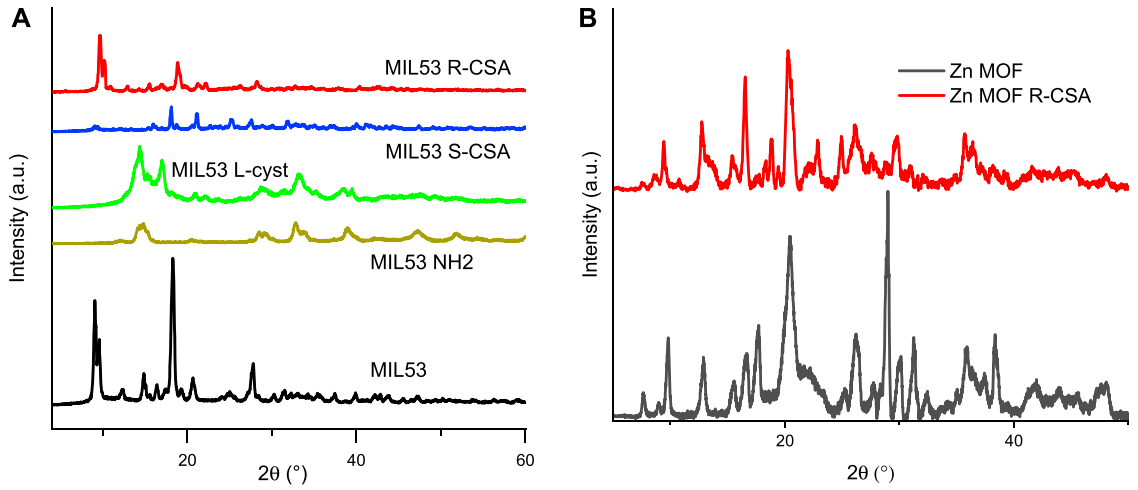

FIGURE 3
Powder XRD. **(A)** MIL53 and MIL 53 R-CSA and comparison with the simulated ones from literature single crystals structures of the MIL53 in the hydrated and dehydrated form **(B)** Zn-MOF and Zn-MOF R-CSA.

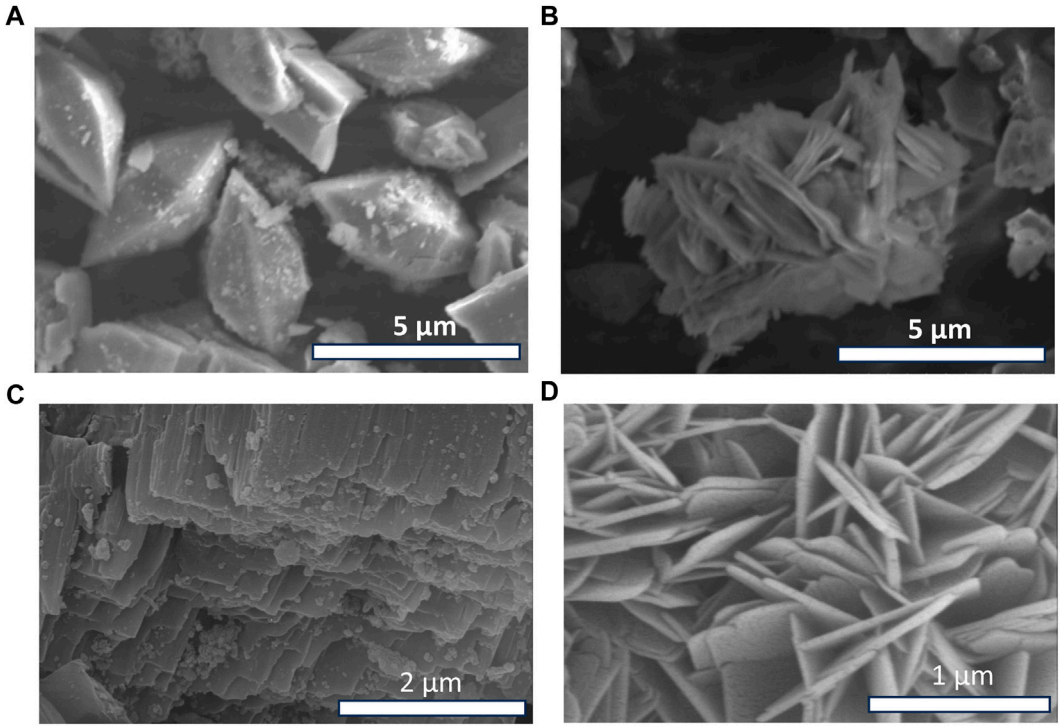

FIGURE 4
SEM images: **(A)** MIL53 **(B)** Zn-MOF. High resolution FESEM images: **(C)** MIL53 **(D)** Zn-MOF.

3.2 Vibrational IR spectroscopy results

Figure 2A shows the IR spectra of the reference MIL-53(Fe) MOF and chiral MIL-53(Fe) based MOFs, synthesized by including chiral linkers. The IR spectrum of MIL-53 (black line) shows the characteristic absorption peaks of MIL53(Fe) shows the characteristic absorption peaks of MIL53 were obviously observed at 1,668, 1,546, 1,391, 750, and the doublets 552/523 cm^{-1}. These values are in agreement with those reported in the literature for iron-based MOFs (Banerjee et al., 2012). In detail, the peak observed at 1,668 cm^{-1} is assigned to the carboxylic C=O bonds stretching vibration confirming the absence of free ligand in the synthesized MIL53 sample. Indeed, the free ligand MIL53 precursor H_2BDC shows the carboxylic C=O stretching at about 1,680 cm^{-1}, the

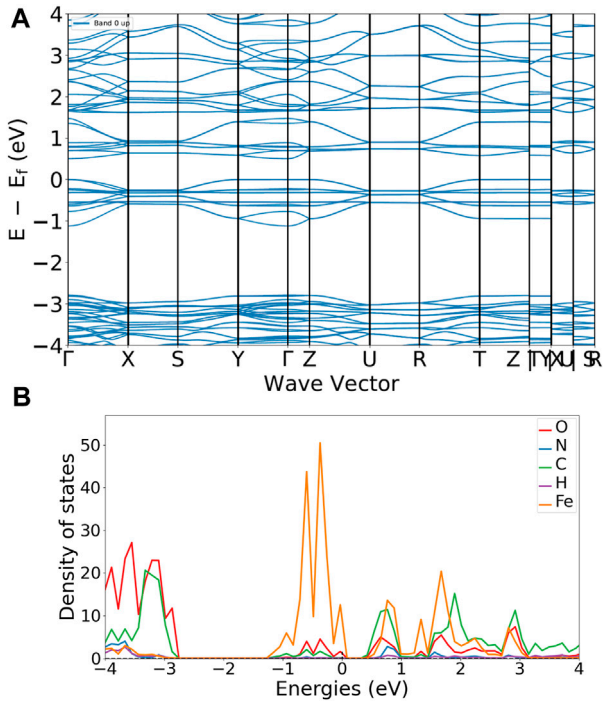

FIGURE 5
MIL53 reference, quantum espresso results. **(A)** band *versus* wave vector plot. **(B)** projected density of state for the atoms in the MIL53 MOF framework.

decrease in energy confirms the interaction of the ligand with the Fe of the network (Li et al., 2018). The two intense peaks charactering the IR spectrum at 1,546 and 1,391 cm^{-1} instead correspond to the asymmetric and symmetric vibrations of the C-O of the two carboxyl groups of the H_2BDC ligand, respectively. The intense and sharp peak at 750 cm^{-1} is assigned to the aromatic C-H bending of the benzene ring. These results confirm the presence of the dicarboxylate linker within frameworks (Yang et al., 2016). The bands in the fingerprint region, between 700 and 400 cm^{-1}, are ascribed to the stretching vibration of Fe–O, indicating the formation of a Fe-oxo bond between the Fe(III) and the carboxylic group of BDC ligand (Gong et al., 2002). NH2 MIL53 shows the same spectral pattern and more features in the range 3,300–3,500 cm^{-1} which belongs to the N-H stretching of the amino group of the amino-terephthalic acid used for its synthesis. The presence of the amino group on the benzenic ring of the terephthalic acid shifts the C-H bending peak from 750 cm^{-1} of the MIL53 to higher energy at 769 cm^{-1}. MIL53 MOFs synthesized with chiral ligands, L-cyst, R-CSA and S-CSA, all show the same peaks as described above with the confirmation of the Fe-O bond formation by the peak at 552 cm^{-1}. The IR spectra of the Zinc based MOFs (Figure 2B) shows the typical structure due to the carboxylic moiety in the 1,300 to 1,600 cm^{-1} range, even if Zn MOFs spectra are not as well defined as the MIL53 ones. A peak in the fingerprint region, at 431cm^{-1} can be attributed to the Zn-O bond, the peaks observed at 811 cm^{-1}, and 1,043 cm^{-1}, can be N-H wag and a C-N stretch. ZnMOF-NH_2 and ZnMOF L Cysteine show a peak between 3,300 cm^{-1}, and 3,400 cm^{-1}, which can be attributed to N-H stretching. Of interest is, when comparing the Zn MOF spectra and the derivatives, the peak observed at 1923 cm^{-1} has undergone a red shift and can now be observed at 2081cm^{-1} in Zn MOF S-CSA and Zn MOF L Cysteine. This shift can be attributed to the formation of hydrogen bonds between the chiral linkers and the linker N,N'-bis(pyridin-4-methyl)cyclohexane-1,4-diamine.

Indeed, there is also a neat difference in the morphological aspect between the iron based and zinc based MOFs; and the crystal structure of the Zn based MOFs is definitively much more disordered than that of the iron based ones.

3.3 Structural results

Since its first synthesis MIL53 has shown some analogies with the other MIL-MOFs based on other metallic cations such as Cr^{3+} (Serre et al., 2002) and Al^{3+} (Loiseau et al., 2004) materials MIL53(Cr) and MIL53(Al) but X-ray showed that they are not isostructural. MIL53(Fe) is built up from corner-sharing trans chains of octahedral Fe linked together by benzene-dicarboxylate (BDC) moieties forming an open framework with channels parallel to the crystallographic c-axis. MIL53 shows a peculiar nature presenting a reversible phase transition between the hydrated and the dehydrated form at near room temperature (below 330 K) (Millange et al., 2008).

Figure 3 sets out X-ray diffraction pattern of iron and Zn MOFs. In particular, Figure 3A reports the comparison between the powder XRD of the MIL53 and MIL53 R-CSA synthesized in the present work and the simulated ones form the literature crystal structure of the two hydrated and dehydrated form of MIL53. MIL53 and MIL53 R-CSA synthesized in this work appear to be a mixture of dehydrated form, as for the presence of the diffraction peak at about 12.7 (°), and of the hydrated form, for matching the peak at 19 (°). Indeed, the reference MIL53 and the CSA doped MOFs result rather similar. From the tight comparison of XRD patterns shown in Figure 3, we can infer that iron is in its usual octahedral (complexed by oxygen) site coordination, and that CSA does not destroy or alter in a significant way the MOF framework, but rather occupies interstitial free space within the MOF framework (see Supplementary Figure S5 for the molecular iron and zinc based MOFs structure).

3.4 SEM and EDS composition

Figure 4 shows SEM images of iron-based MIL53 and zinc-based MOF. In the two cases the morphology appears different. MIL53 shows a regular morphology while Zn-MOF shows a lamellar morphology. In both cases, the presence of structures of less than 5 μm is observed. The chiral variants of MIL53 show similar structures to that of MIL53 while NH2 MIL53 is instead organised in more spherical structures, all images are shown in Supplementary Figures S6–S10. Zn-MOF R-CSA and Zn-MOF S-CSA show the typical lamellar structure of Zn-MOF differently, the lamellar structure is less visible in NH2 Zn-MOF and Zn-MOF L-Cys. All SEM images of Zn-MOF are shown in Supplementary Figures S11–S15. EDS spectra performed on the MOF powder are shown in Sections 6 and 7 of the supporting information. In particular, EDS spectra

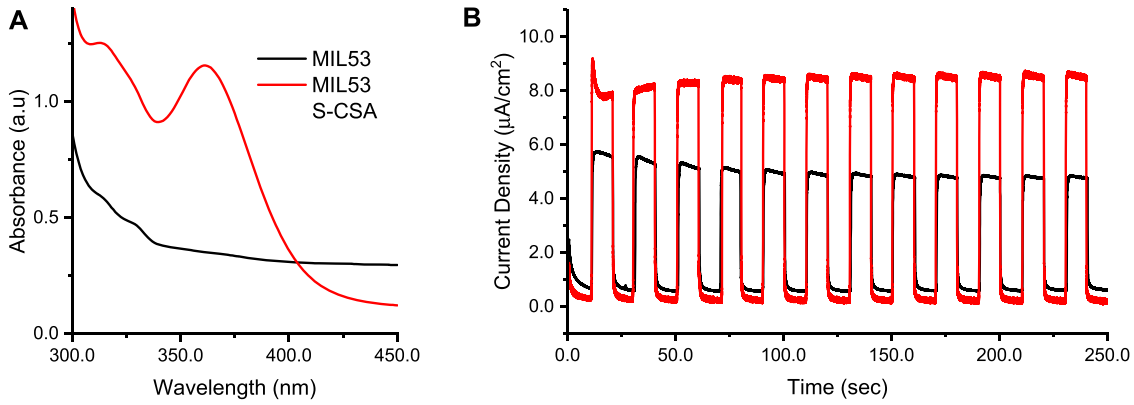

FIGURE 6
Photoelectrochemical results of FTO/TiO_2/MIL53 and FTO/TiO_2/MIL53 S-CSA working electrodes, Pt wire the CE, Ag/$AgKCl_{sat}$the RE, 0.1 M sodium sulphate aqueous solution. **(A)** UV-Vis spectra: black line the MIL53, red line the MIL53 S-CSA. **(B)** Chronoamperometry recorded at constant 1.0 V potential under chopped, 20 s for the whole on/off single cycle, AM1.5g illumination: black line the MIL53, red line the MIL53 S-CSA.

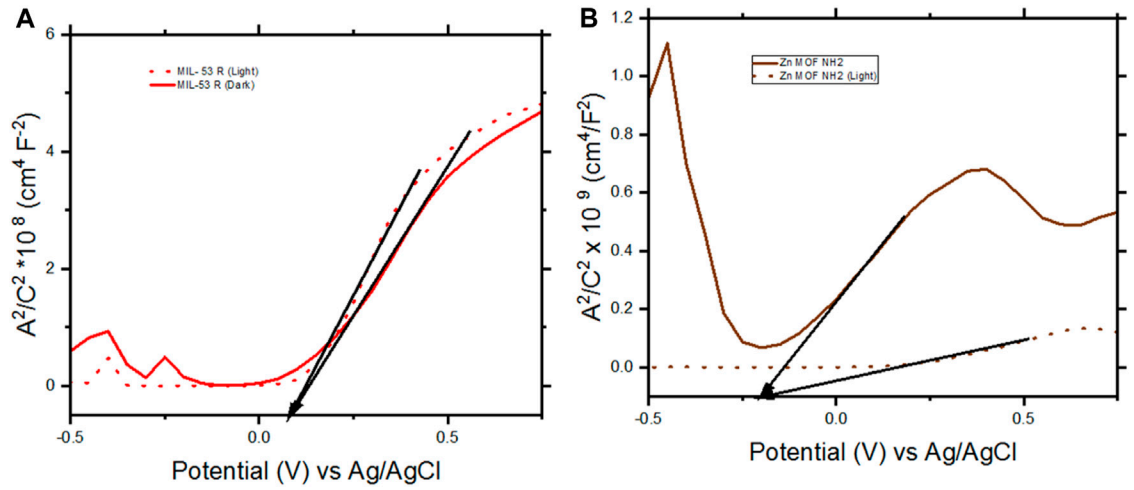

FIGURE 7
Mott- Schottky results of FTO/TiO_2/MIL53 R-CSA and FTO/TiO_2/Zn MOF NH_2 working electrodes. **(A)** FTO/TiO_2/MIL53 R-CSA. **(B)** FTO/TiO_2/Zn MOF NH_2. The measurements were performed while sweeping voltages from 0.75 V to −0.5 V using an AC Voltage with an amplitude of 5 mV and frequency of 1,000 Hz, under illumination and under darkness.

make it possible to find the chemical composition of MOFs (expressed as an atomic percentage). Note that in the MIL53-type structures, the presence of iron is noted. In the chiral variants MIL53 L-Cys, MIL53 R-CSA, MIL53 S-CSA, EDS analysis confirms the presence of sulphur (element present in cysteine and camphor sulfonic acid doping molecules). Similar considerations can be made for Zn-MOF, in which Zn is observed. The EDS analysis on the chiral variants Zn-MOF L-Cys, Zn-MOF R-CSA and Zn-MOF S-CSA show the signal related to the presence of sulphur. Figures 4C, D show high resolution FE-SEM images of MIL53 and Zn-MOF, respectively. In the case of MIL53 emerges a morphology rather different from the low resolution one: the octahedral-like shape of the MIL53 crystals show a lamellar substructure revealing a layer substructure.

3.5 Theoretical results

Quantum mechanical based calculations are carried out to compare the electronic structure information gained by the electrochemical analysis as a function of the MOFs molecular structure, Figure 5. Calculations have been performed using, both localized orbitals and plane wave DFT methods. Figure 5A shows a typical band energy *versus* wave vector plot. Focusing on the boundary between the valence and conduction band (close to the Fermi energy, Ef) a band gap of about 0.5 eV is found, which is in reasonable agreement with the results obtained in the case of solid state electrochemistry investigations dealing with organic charge transfer crystals (Solano et al., 2021; Solano et al., 2022). The relevant density of state (DOS) plot, Figure 5B, gives due reason to the role of iron in the CV results. In that, the projected DOS (pDOS) plot shows

a maximum localization on iron. Please compare the orange peaks around the Fermi energy.

Also localized orbitals calculations yield a picture widely in agreement with results obtained by using plane wave basis with periodic boundary constraints. The Mulliken net charge on iron is positive and both the HOMO and LUMO are delocalized between the centra iron and the oxygens of the carboxylic groups coordinating the iron (compare Section 8 of the supporting information). In tight agreement with the experimental electrochemical results which indicate that the quasi-reversible current peaks evident in the CV curves are due to the iron oxidation in the forward curve.

3.6 Photo-electrochemical water splitting

The MOFs synthesized here, supported on titania, were used as working electrode in the water splitting process, in a photo-electrochemical experiment. In particular, MOFs supported on titania served as the working electrode (anode) for the oxygen evolution reaction (OER). MIL53 S-CSA was selected as a candidate for photo-electrochemical measurements, because of CV and UV-Vis results. UV-Vis spectra of MIL53 and Zn-MOF are reported in Supplementary Figures S16, S17 respectively. Chronoamperometry curves (current vs. time) at constant 1.0 V potential under illumination of an AM1.5G solar simulator were recorded. Supplementary Figure S18 shows the Air Mass (AM) experimental spectrum used as excited light source in photoelectrochemical experiments. To investigate the effect of photo-excitation, dark and light conditions were obtained by chopping the light source ON and OFF, in 20 s intervals between light-ON and light-OFF single cycles. Figure 6A sets out the absorption UV-Vis spectra of both MIL53 (black line) as a reference, and the chiralized MIL53 S-CSA (red line), Figure 6B shows current vs. time chronoamperometry curves. 1.0 V was selected as a potential close to the onset of the OER, but still without oxygen evolution. Figure 6B shows that the chiralized MIL53 S-CSA is characterized by a substantial increase in the photocurrent (light on) with respect to the achiral one. On one side, the advantage of the chiralized MIL53 S-CSA is due to the larger absorption with respect to the achiral MIL53, as depicted in Figure 6A. MIL53 S-CSA takes advantage of both being a more efficient light antenna and as a spin-filter (being chiral) as a result the OER reaction is catalyzed. All in all, this outcome is consistent with results present in the literature, where the redox processes concerning the oxygen are shown to be sensitive to the handedness of the electrode surface via chirality-spin interaction (Mtangi et al., 2015; Mtangi et al., 2017; Gazzotti et al., 2020; Sang et al., 2022).

From literature cited above, it has been noted when chiral photoelectrodes are used in photoelectrochemical water splitting, there is spin filtering of the transmitted electrons i.e., there is preferential transmission of electrons spinning one direction. When there is electron spin filtering, the formation of triplet oxygen ($^3O_2$) is promoted, while formation of hydrogen peroxide is minimised. When the formation of hydrogen peroxide is minimized the yield of hydrogen improves, this can also be correlated to the current densities produced by achiral MIL-53 vs. MIL53 doped with R CSA.

During water splitting, Mott-Schottky analysis was carried out to determine the electronic properties of the photoelectrodes (Figure 7). The measurements were performed while sweeping voltages from 0.75 V to −0.5 V using an AC Voltage with an amplitude of 5 mV and frequency of 1000 Hz. Measurements were carried out under illumination and under darkness.

The flat band potentials for MIL 53 R-CSA under illumination and under darkness are similar at + 0.08 V, while for Zn MOF NH_2 the flat band potentials are – 0.19 V, due to the fact that the flat band potentials are similar, we can conclude that the molecules did not affect the electronic properties of the TiO_2 and that the observed current densities, were due to the activity of the molecules deposited.

4 Conclusion

MOFs of the MIL53 class have been synthesized and "doped" with a small amount of four different organic compounds: achiral amino terephthalic acid, enantiopure S-CSA, R-CSA and L-cysteine. Structural characterization indicates that the organic "dopants" do not interfere with the MOF framework, but rather occupy interstitial sites within the MOF framework, i.e. a sort of "supermolecular" architecture. Nonetheless, "dopants" affects the electronic structure of the MOF, as it is suggested by the variation of redox potentials of the Fe(III)/Fe(II) couple in CV curves. Eventually, DFT theoretical calculations yield an overall picture in agreement with these experimental evidences. It is definitively worth of further investigation the "strong" influence of L-cysteine on the electronic properties of the MOF, as it is substantiated by the major variation in the CV redox current peaks, yielding a splitting of the peak into two broad swallow peaks. Eventually, photoelectrochemical results show that the "chiral" doping, MIL53 S-CSA, leads to a substantial increase in the OER photocurrent, this result seems due to the role of chiral electrode surfaces in the oxygen redox process. (Mtangi et al., 2015; Mtangi et al., 2017; Sang et al., 2022).

Data availability statement

The raw data supporting the conclusion of this article will be made available by the authors, without undue reservation.

Author contributions

Conceptualization, RK, MB, EV, MI, CF, GM, and WM; formal analysis, WG, EV, and IM; investigation, RK, MB, IM, TS, and DM; writing—original draft preparation, MB, CF; writing—review and editing, MB, MI, and WM; funding acquisition, MI, CF, and WM. All authors contributed to the article and approved the submitted version.

Funding

Part of this work was carried with the aid of a grant from UNESCO-TWAS and Swedish International Development Cooperation Agency (Sida) for Individual Scientist Grant No. 21-303 RG/PHYS/AF/AC_G-FR3240319510. The views expressed herein do not necessarily represent those of UNESCO-TWAS, Sida or its Board of Governors. "WM acknowledges financial support from PhosAgro/UNESCO/IUPAC for Green Chemistry: "Hydrogen generation through photoelectrocatalytic

water splitting" Grant No. 4500415755. CF gratefully thanks financial support from Dipartimento di Ingegneria "Enzo Ferrari" (DIEF), UniMORE, FARD 2021—linea di azione di tipo 3: "Materiali chirali per batterie al litio e celle a combustibile" and from Consorzio Interuniversitario Nazionale per la Scienza e Tecnologia dei Materiali (INSTM), fondi triennali: "INSTM21MOFONTANESI",TWAS UNESCO Expert Visiting Program, RF number 3240322698".

Conflict of interest

The authors declare that the research was conducted in the absence of any commercial or financial relationships that could be construed as a potential conflict of interest.

Publisher's note

Supplementary material

The Supplementary Material for this article can be found online at: https://www.frontiersin.org/articles/10.3389/fchem.2023.1215619/full#supplementary-material

References

Abbas, A., Wang, Z.-X., Li, Z., Jiang, H., Liu, Y., Cui, Y. (2018). Enantioselective separation over a chiral biphenol-based metal–organic framework. *Inorg. Chem.* 57, 8697–8700. doi:10.1021/acs.inorgchem.8b00948

Ajpi, C., Leiva, N., Lundblad, A., Lindbergh, G., Cabrera, S. (2023). Synthesis and spectroscopic characterization of Fe3+-BDC metal organic framework as material for lithium ion batteries. *J. Mol. Struct.* 1272, 134127. doi:10.1016/j.molstruc.2022.134127

Altaf, A., Hassan, S., Pejcic, B., Baig, N., Hussain, Z., Sohail, M. (2022). Recent progress in the design, synthesis and applications of chiral metal-organic frameworks. *Front. Chem.* 10, 1014248. doi:10.3389/fchem.2022.1014248

Altaf, M., Sohail, M., Mansha, M., Iqbal, N., Sher, M., Fazal, A., et al. (2018). Synthesis, characterization, and photoelectrochemical catalytic studies of a water-stable zinc-based metal–organic framework. *ChemSusChem* 11, 542–546. doi:10.1002/cssc.201702122

Andrienko, G. A. (2023). Chemcraft - graphical software for visualization of quantum chemistry computations. Available at: https://www.chemcraftprog.com.

Banerjee, A., Gokhale, R., Bhatnagar, S., Jog, J., Bhardwaj, M., Lefez, B., et al. (2012). MOF derived porous carbon–Fe3O4 nanocomposite as a high performance, recyclable environmental superadsorbent. *J. Mater. Chem.* 22, 19694–19699. doi:10.1039/c2jm33798c

Berretti, E., Calisi, N., Capaccioli, A., Capozzoli, L., Hamouda, A. M. S., Giaccherini, A., et al. (2020). Electrodeposited white bronzes on brass: Corrosion in 3.5 % sodium chloride solution. *Corros. Sci.* 175, 108898. doi:10.1016/j.corsci.2020.108898

Bhattacharjee, S., Khan, M., Li, X., Zhu, Q.-L., Wu, X.-T. (2018). Recent progress in asymmetric catalysis and chromatographic separation by chiral metal–organic frameworks. *Catalysts* 8, 120. doi:10.3390/catal8030120

Bonechi, M., Giurlani, W., Stefani, A., Marchetti, A., Innocenti, M., Fontanesi, C. (2022). Resorcinol electropolymerization process obtained via electrochemical oxidation. *Electrochim. Acta* 428, 140928. doi:10.1016/j.electacta.2022.140928

Bonechi, M., Giurlani, W., Vizza, M., Savastano, M., Stefani, A., Bianchi, A., et al. (2021a). On the oxygen reduction reaction mechanism catalyzed by Pd complexes on 2D carbon. A theoretical study. *Catalysts* 11, 764. doi:10.3390/catal11070764

Bonechi, M., Innocenti, M., Vanossi, D., Fontanesi, C. (2021b). The fundamental and underrated role of the base electrolyte in the polymerization mechanism. The resorcinol case study. *J. Phys. Chem. A* 125, 34–42. doi:10.1021/acs.jpca.0c07702

Chen, D., Chen, S., Jiang, Y., Xie, S., Quan, H., Hua, L., et al. (2017). Heterogeneous Fenton-like catalysis of Fe-MOF derived magnetic carbon nanocomposites for degradation of 4-nitrophenol. *RSC Adv.* 7, 49024–49030. doi:10.1039/c7ra09234b

Comparini, A., Del Pace, I., Giurlani, W., Emanuele, R., Verrucchi, M., Bonechi, M., et al. (2023). Electroplating on Al6082 aluminium: A new green and sustainable approach. *Coatings* 13, 13. doi:10.3390/coatings13010013

Cossi, M., Rega, N., Scalmani, G., Barone, V. (2003). Energies, structures, and electronic properties of molecules in solution with the C-PCM solvation model. *J. Comput. Chem.* 24, 669–681. doi:10.1002/jcc.10189

Daniel, M., Mathew, G., Anpo, M., Neppolian, B. (2022). MOF based electrochemical sensors for the detection of physiologically relevant biomolecules: An overview. *Coord. Chem. Rev.* 468, 214627. doi:10.1016/j.ccr.2022.214627

Dybtsev, D. N., Bryliakov, K. P. (2021). Asymmetric catalysis using metal-organic frameworks. *Coord. Chem. Rev.* 437, 213845. doi:10.1016/j.ccr.2021.213845

Forni, F., Innocenti, M., Pezzatini, G., Foresti, M. L. (2000). Electrochemical aspects of CdTe growth on the face (111) of silver by ECALE. *Electrochim. Acta* 45, 3225–3231. doi:10.1016/s0013-4686(00)00426-6

Frisch, M. J., Trucks, G. W., Schlegel, H. B., Scuseria, G. E., Robb, M. A., Cheeseman, J. R., et al. 2017.

Garcés-Pineda, F. A., Blasco-Ahicart, M., Nieto-Castro, D., López, N., Galán-Mascarós, J. R. (2019). Direct magnetic enhancement of electrocatalytic water oxidation in alkaline media. *Nat. Energy* 4, 519–525. doi:10.1038/s41560-019-0404-4

Gazzotti, M., Stefani, A., Bonechi, M., Giurlani, W., Innocenti, M., Fontanesi, C. (2020). Influence of chiral compounds on the oxygen evolution reaction (OER) in the water splitting process. *Molecules* 25, 3988. doi:10.3390/molecules25173988

Gedrich, K., Heitbaum, M., Notzon, A., Senkovska, I., Fröhlich, R., Getzschmann, J., et al. (2011). A family of chiral metal-organic frameworks. *Chem. Eur. J.* 17, 2099–2106. doi:10.1002/chem.201002568

Ghanbari, T., Abnisa, F., Wan Daud, W. M. A. (2020). A review on production of metal organic frameworks (MOF) for CO2 adsorption. *Sci. Total Environ.* 707, 135090. doi:10.1016/j.scitotenv.2019.135090

Gheorghe, A., Reus, S., Koenis, M., Dubbeldam, D., Woutersen, S., Tanase, S. (2021). Role of additives and solvents in the synthesis of chiral isoreticular MOF-74 topologies. *Dalton Trans.* 50, 12159–12167. doi:10.1039/d1dt01945g

Giannozzi, P., Baroni, S., Bonini, N., Calandra, M., Car, R., Cavazzoni, C., et al. (2009). Quantum espresso: A modular and open-source software project for quantum simulations of materials. *J. Phys. Condens. Matter* 21, 395502. doi:10.1088/0953-8984/21/39/395502

Giurlani, W., Cavallini, M., Picca, R. A., Cioffi, N., Passaponti, M., Fontanesi, C., et al. (2020). Underpotential-Assisted electrodeposition of highly crystalline and smooth thin film of bismuth. *ChemElectroChem* 7, 299–305. doi:10.1002/celc.201901678

Giurlani, W., Giaccherini, A., Calisi, N., Zangari, G., Salvietti, E., Passaponti, M., et al. (2018). Investigations on the electrochemical atomic layer growth of Bi2Se3 and the surface limited deposition of bismuth at the silver electrode. *Materials* 11, 1426. doi:10.3390/ma11081426

Giurlani, W., Sergi, L., Crestini, E., Calisi, N., Poli, F., Soavi, F., et al. (2022b). Electrochemical stability of steel, Ti, and Cu current collectors in water-in-salt electrolyte for green batteries and supercapacitors. *J. Solid State Electrochem* 26, 85–95. doi:10.1007/s10008-020-04853-2

Giurlani, W., Vizza, M., Pizzetti, F., Bonechi, M., Savastano, M., Sorace, L., et al. (2022a). Magnetic field effect on the handedness of electrodeposited heusler alloy. *Appl. Sci.* 12, 5640. doi:10.3390/app12115640

Gonçalves, J. M., Martins, P. R., Rocha, D. P., Matias, T. A., Julião, M. S. S., Munoz, R. A. A., et al. (2021). Recent trends and perspectives in electrochemical sensors based on MOF-derived materials. *J. Mater. Chem. C* 9, 8718–8745. doi:10.1039/d1tc02025k

Gong, C., Chen, D., Jiao, X., Wang, Q. (2002). Continuous hollow α-Fe2O3 and α-Fe fibers prepared by the sol–gel method. *J. Mater. Chem.* 12, 1844–1847. doi:10.1039/b201243j

Gong, W., Chen, Z., Dong, J., Liu, Y., Cui, Y. (2022). Chiral metal–organic frameworks. *Chem. Rev.* 122, 9078–9144. doi:10.1021/acs.chemrev.1c00740

Guo, H., Wang, D., Chen, J., Weng, W., Huang, M., Zheng, Z. (2016). Simple fabrication of flake-like NH 2 -MIL-53(Cr) and its application as an electrochemical sensor for the detection of Pb 2+. *Chem. Eng. J.* 289, 479–485. doi:10.1016/j.cej.2015.12.099

Han, Z., Wang, K., Guo, Y., Chen, W., Zhang, J., Zhang, X., et al. (2019). Cation-induced chirality in a bifunctional metal-organic framework for quantitative enantioselective recognition. *Nat. Commun.* 10, 5117. doi:10.1038/s41467-019-13090-9

Innocenti, M., Pezzatini, G., Forni, F., Foresti, M. L. (2001). CdS and ZnS deposition on Ag(111) by electrochemical atomic layer epitaxy. *J. Electrochem. Soc.* 148, C357. doi:10.1149/1.1360208

James, S. L. (2003). Metal-organic frameworks. *Chem. Soc. Rev.* 32, 276. doi:10.1039/b200393g

Jiang, Y., Zhao, H., Yue, L., Liang, J., Li, T., Liu, Q., et al. (2021). Recent advances in lithium-based batteries using metal organic frameworks as electrode materials. *Electrochem. Commun.* 122, 106881. doi:10.1016/j.elecom.2020.106881

Kutzscher, C., Müller, P., Raschke, S., Kaskel, S. (2016).*The Chemistry of metal-organic frameworks: Synthesis, characterization, and applications*. Editor S. Kaskel (Weinheim, Germany: Wiley-VCH Verlag GmbH and Co. KGaA), 387–419.

Le, T., Cowan, M., Drobek, M., Bechelany, M., Julbe, A., Cretin, M. (2019). Fe-nanoporous carbon derived from MIL-53(Fe): A heterogeneous catalyst for mineralization of organic pollutants. *Nanomaterials* 9, 641. doi:10.3390/nano9040641

Li, R., Chen, Z., Cai, M., Huang, J., Chen, P., Liu, G., et al. (2018). Improvement of Sulfamethazine photodegradation by Fe(III) assisted MIL-53(Fe)/percarbonate system. *Appl. Surf. Sci.* 457, 726–734. doi:10.1016/j.apsusc.2018.06.294

Li, X., Sun, Q., Liu, J., Xiao, B., Li, R., Sun, X. (2016). Tunable porous structure of metal organic framework derived carbon and the application in lithium–sulfur batteries. *J. Power Sources* 302, 174–179. doi:10.1016/j.jpowsour.2015.10.049

Loiseau, T., Serre, C., Huguenard, C., Fink, G., Taulelle, F., Henry, M., et al. (2004). A rationale for the large breathing of the porous aluminum terephthalate (MIL-53) upon hydration. *Chem. Eur. J.* 10, 1373–1382. doi:10.1002/chem.200305413

Ma, M., Chen, J., Liu, H., Huang, Z., Huang, F., Li, Q., et al. (2022). A review on chiral metal–organic frameworks: Synthesis and asymmetric applications. *Nanoscale* 14, 13405–13427. doi:10.1039/d2nr01772e

Ma, T., Li, H., Ma, J.-G., Cheng, P. (2020). Application of MOF-based materials in electrochemical sensing. *Dalton Trans.* 49, 17121–17129. doi:10.1039/d0dt03388j

Mariani, E., Giurlani, W., Bonechi, M., Dell'Aquila, V., Innocenti, M. (2022). A systematic study of pulse and pulse reverse plating on acid copper bath for decorative and functional applications. *Sci. Rep.* 12, 18175. doi:10.1038/s41598-022-22650-x

Millange, F., Guillou, N., Walton, R. I., Grenèche, J.-M., Margiolaki, I., Férey, G. (2008). Effect of the nature of the metal on the breathing steps in MOFs with dynamic frameworks. *Chem. Commun.*, 4732–4734. doi:10.1039/b809419e

Millange, F., Walton, R. I. (2018). MIL-53 and its isoreticular analogues: A review of the chemistry and structure of a prototypical flexible metal-organic framework. *Isr. J. Chem.* 58, 1019–1035. doi:10.1002/ijch.201800084

Mtangi, W., Kiran, V., Fontanesi, C., Naaman, R. (2015). Role of the electron spin polarization in water splitting. *J. Phys. Chem. Lett.* 6, 4916–4922. doi:10.1021/acs.jpclett.5b02419

Mtangi, W., Tassinari, F., Vankayala, K., Vargas Jentzsch, A., Adelizzi, B., Palmans, A. R. A., et al. (2017). Control of electrons' spin eliminates hydrogen peroxide formation during water splitting. *J. Am. Chem. Soc.* 139, 2794–2798. doi:10.1021/jacs.6b12971

Mukhopadhyay, S., Basu, O., Nasani, R., Das, S. K. (2020). Evolution of metal organic frameworks as electrocatalysts for water oxidation. *Chem. Commun.* 56, 11735–11748. doi:10.1039/d0cc03659e

Navarathna, C. M., Dewage, N. B., Karunanayake, A. G., Farmer, E. L., Perez, F., Hassan, E. B., et al. (2020). Rhodamine B adsorptive removal and photocatalytic degradation on MIL-53-Fe MOF/magnetic magnetite/biochar composites. *J. Inorg. Organomet. Polym.* 30, 214–229. doi:10.1007/s10904-019-01322-w

Niu, X., Yan, S., Chen, J., Li, H., Wang, K. (2022). Enantioselective recognition of L/D-amino acids in the chiral nanochannels of a metal-organic framework. *Electrochim. Acta* 405, 139809. doi:10.1016/j.electacta.2021.139809

Nivetha, R., Kollu, P., Chandar, K., Pitchaimuthu, S., Jeong, S. K., Grace, A. N. (2019). Role of MIL-53(Fe)/hydrated–dehydrated MOF catalyst for electrochemical hydrogen evolution reaction (HER) in alkaline medium and photocatalysis. *RSC Adv.* 9, 3215–3223. doi:10.1039/c8ra08208a

Padmanaban, M., Müller, P., Lieder, C., Gedrich, K., Grünker, R., Bon, V., et al. (2011). Application of a chiral metal–organic framework in enantioselective separation. *Chem. Commun.* 47, 12089. doi:10.1039/c1cc14893a

Passaponti, M., Lari, L., Bonechi, M., Bruni, F., Giurlani, W., Sciortino, G., et al. (2020). Optimisation study of Co deposition on chars from MAP of waste tyres as green electrodes in ORR for alkaline fuel cells. *Energies* 13, 5646. doi:10.3390/en13215646

Peng, Y., Gong, T., Zhang, K., Lin, X., Liu, Y., Jiang, J., et al. (2014). Engineering chiral porous metal-organic frameworks for enantioselective adsorption and separation. *Nat. Commun.* 5, 4406. doi:10.1038/ncomms5406

Salvietti, E., Giurlani, W., Foresti, M., Passaponti, M., Fabbri, L., Marcantelli, P., et al. (2018). On the contrasting effect exerted by a thin layer of CdS against the passivation of silver electrodes coated with thiols. *Surfaces* 1, 29–42. doi:10.3390/surfaces1010004

Sang, Y., Tassinari, F., Santra, K., Zhang, W., Fontanesi, C., Bloom, B. P., et al. (2022). *PNAS* 119, e2202650119.

Savastano, M., Passaponti, M., Giurlani, W., Lari, L., Bianchi, A., Innocenti, M. (2020). Multi-walled carbon nanotubes supported Pd(II) complexes: A supramolecular approach towards single-ion oxygen reduction reaction catalysts. *Energies* 13, 5539. doi:10.3390/en13215539

Sawano, T., Thacker, N. C., Lin, Z., McIsaac, A. R., Lin, W. (2015). Robust, chiral, and porous BINAP-based metal–organic frameworks for highly enantioselective cyclization reactions. *J. Am. Chem. Soc.* 137, 12241–12248. doi:10.1021/jacs.5b09225

Scherb, C., Schödel, A., Bein, T. (2008). Directing the structure of metal–organic frameworks by oriented surface growth on an organic monolayer. *Angew. Chem. Int. Ed.* 47, 5777–5779. doi:10.1002/anie.200704034

Serre, C., Millange, F., Thouvenot, C., Noguès, M., Marsolier, G., Louër, D., et al. (2002). Very large breathing effect in the first nanoporous chromium(III)-Based solids: MIL-53 or $Cr^{III}(OH)\cdot\{O_2C–C_6H_4–CO_2\}\cdot\{HO_2C–C_6H_4–CO_2H\}_x\cdot H_2O_y$. *J. Am. Chem. Soc.* 124, 13519–13526. doi:10.1021/ja0276974

Sharifzadeh, Z., Berijani, K., Morsali, A. (2021). Chiral metal–organic frameworks based on asymmetric synthetic strategies and applications. *Coord. Chem. Rev.* 445, 214083. doi:10.1016/j.ccr.2021.214083

Solano, F., Inaudi, P., Abollino, O., Giacomino, A., Chiesa, M., Salvadori, E., et al. (2022). Charge transfer modulation in charge transfer co-crystals driven by crystal structure morphology. *Phys. Chem. Chem. Phys.* 24, 18816–18823. doi:10.1039/d2cp01408d

Solano, F., Inaudi, P., Chiesa, M., Kociok-Köhn, G., Salvadori, E., Da Como, E., et al. (2021). Spin multiplicity and solid-state electrochemical behavior in charge-transfer Co-crystals of DBTTF/F4TCNQ. *J. Phys. Chem. C* 125, 8677–8683. doi:10.1021/acs.jpcc.1c00020

Stefani, A., Giurlani, W., Bonechi, M., Marchetti, A., Preda, G., Pasini, D., et al. (2021). On the savéant's concerted/stepwise model. The electroreduction of halogenated naphthalene derivatives as a case study. *ChemElectroChem* 8, 4337–4344. doi:10.1002/celc.202100978

Sudik, A. C., Côté, A. P., Yaghi, O. M. (2005). Metal-organic frameworks based on trigonal prismatic building blocks and the new "acs" topology. *Inorg. Chem.* 44, 2998–3000. doi:10.1021/ic050064g

Tran, H. V., Dang, H. T. M., Tran, L. T., Van Tran, C., Huynh, C. D. (2020). Metal-organic framework MIL-53(Fe): Synthesis, electrochemical characterization, and application in development of a novel and sensitive electrochemical sensor for detection of cadmium ions in aqueous solutions. *Adv. Polym. Technol.* 2020, 1–10. doi:10.1155/2020/6279278

Wanderley, M. M., Wang, C., Wu, C.-D., Lin, W. (2012). A chiral porous metal–organic framework for highly sensitive and enantioselective fluorescence sensing of amino alcohols. *J. Am. Chem. Soc.* 134, 9050–9053. doi:10.1021/ja302110d

Wang, C., Zheng, M., Lin, W. (2011). Asymmetric catalysis with chiral porous metal–organic frameworks: Critical issues. *J. Phys. Chem. Lett.* 2, 1701–1709. doi:10.1021/jz200492d

Wang, Q., Astruc, D. (2020). State of the art and prospects in metal–organic framework (MOF)-Based and MOF-derived nanocatalysis. *Chem. Rev.* 120, 1438–1511. doi:10.1021/acs.chemrev.9b00223

Xue, M., Li, B., Qiu, S., Chen, B. (2016). Emerging functional chiral microporous materials: Synthetic strategies and enantioselective separations. *Mater. Today* 19, 503–515. doi:10.1016/j.mattod.2016.03.003

Yang, M., Zhou, Y.-N., Cao, Y.-N., Tong, Z., Dong, B., Chai, Y.-M. (2020). Advances and challenges of Fe-MOFs based materials as electrocatalysts for water splitting. *Appl. Mater. Today* 20, 100692. doi:10.1016/j.apmt.2020.100692

Yang, Q., Liu, Y., Ou, H., Li, X., Lin, X., Zeb, A., et al. (2022). Fe-Based metal–organic frameworks as functional materials for battery applications. *Inorg. Chem. Front.* 9, 827–844. doi:10.1039/d1qi01396c

Yang, X.-L., Zang, R.-B., Shao, R., Guan, R.-F., Xie, M.-H. (2021). Chiral UiO-MOFs based QCM sensors for enantioselective discrimination of hazardous biomolecule. *J. Hazard. Mater.* 413, 125467. doi:10.1016/j.jhazmat.2021.125467

Yang, Z., Xu, X., Liang, X., Lei, C., Wei, Y., He, P., et al. (2016). MIL-53(Fe)-graphene nanocomposites: Efficient visible-light photocatalysts for the selective oxidation of alcohols. *Appl. Catal. B Environ.* 198, 112–123. doi:10.1016/j.apcatb.2016.05.041

Zavakhina, M. S., Samsonenko, D. G., Dybtsev, D. N., Fedin, V. P. (2019). Chiral MOF incorporating chiral guests: Structural studies and enantiomer-dependent luminescent properties. *Polyhedron* 162, 311–315. doi:10.1016/j.poly.2019.02.008

Zhang, J., Chen, S., Wu, T., Feng, P., Bu, X. (2008). Homochiral crystallization of microporous framework materials from achiral precursors by chiral catalysis. *J. Am. Chem. Soc.* 130, 12882–12883. doi:10.1021/ja805272j

Zhang, Y., Li, G., Lu, H., Lv, Q., Sun, Z. (2014). Synthesis, characterization and photocatalytic properties of MIL-53(Fe)–graphene hybrid materials. *RSC Adv.* 4, 7594. doi:10.1039/c3ra46706f

Zhao, R., Wu, Y., Liang, Z., Gao, L., Xia, W., Zhao, Y., et al. (2020). Metal–organic frameworks for solid-state electrolytes. *Energy Environ. Sci.* 13, 2386–2403. doi:10.1039/d0ee00153h

Zhao, Y.-W., Wang, Y., Zhang, X.-M. (2017). Homochiral MOF as circular dichroism sensor for enantioselective recognition on nature and chirality of unmodified amino acids. *ACS Appl. Mater. Interfaces* 9, 20991–20999. doi:10.1021/acsami.7b04640

Zhou, H. C., Kitagawa, S. (2014). Metal–organic frameworks (MOFs). *Chem. Soc. Rev.* 43, 5415–5418. doi:10.1039/c4cs90059f